



Electric vehicle battery-ultracapacitor hybrid energy storage system and drivetrain optimization for a real-world urban driving scenario

Ludmila C. A. Silva¹ · Jony J. Eckert¹ · Maria A. M. Lourenço¹ · Fabricio L. Silva¹ · Fernanda C. Corrêa² · Franco G. Dedini¹

Received: 16 November 2019 / Accepted: 31 March 2021 / Published online: 14 April 2021
© The Brazilian Society of Mechanical Sciences and Engineering 2021

Abstract

A battery has normally a high energy density with low power density, while an ultracapacitor has a high power density but a low energy density. Therefore, this paper has been proposed to associate more than one storage technology generating a hybrid energy storage system (HESS), which has battery and ultracapacitor, whose objective is to improve the electric vehicle (EV) driving range. The HESS parameters have been evaluated in a configuration of EV powered by two in-wheel electric motors, coupled straight into the front wheels, and by a unique EM, connected to a differential transmission to drive the rear wheels. Moreover, this paper considers a real-world drive cycle based on the urban driving behavior of Campinas city, one of the most populous cities in Brazil. Aiming to minimize the HESS size and enhance the EV driving range, an optimization problem was formulated and solved using a genetic algorithm technique, in which the EV drivetrain parameters and HESS components and control are optimized. Finally, the obtained Pareto frontier defines the optimum EV configurations, in which the best-selected configurations were able to perform up to 188 km with a 418 kg HESS (maximum drive range solution), or 82.75 km with a 146.58 kg HESS (minimum HESS solution) and 319 km with a 188.43 kg HESS (best trade-off solution), without presenting performance losses.

Keywords Electric vehicle (EV) · Hybrid energy storage system (HESS) · Genetic algorithm optimization · Real-world driving cycle

1 Introduction

The development of electric vehicles (EVs) is a challenge for the automotive industry to face limited fossil fuel sources and environmental issues [1–3], of which a major parcel is generated by vehicles propelled by combustion engines [2, 4, 5]. The main characteristics of EVs are no fuel consumption, little noise and good energy efficiency, which makes the EVs the best alternative to reach zero-pollution mobility

in the future [6]. However, this kind of vehicles needs to attempt some characteristic as low energy consumption, a good range and acceptable driving performance to become competitive in the market [7]. To achieve these goals, the biggest limitation is related to the energy storage systems (ESS), which have a great impact on vehicle range, energy consumption, weight and cost of these vehicles [1].

Batteries are considered a vital component due to its influence on vehicle acceleration and autonomy on a single charge [8]. Although, batteries have drawbacks such as low-power density, compared with other energy storage devices, a high cost and a lower lifetime. Several types of researches have been made to overcome some of these limitations. Batteries cost, energy density, and especially lifetime are decisive for the EV market [9]. The combination of batteries with other storage devices could be relevant to obtain better performance [10]. Therefore, hybrid energy storage systems (HESSs) can be developed by combining batteries, ultracapacitors, flywheel and/or hydrogen cell [11, 12].

Technical Editor: Victor Juliano De Negri.

✉ Ludmila C. A. Silva
ludmila@fem.unicamp.br
Jony J. Eckert
javorski@fem.unicamp.br

¹ Integrated Systems Laboratory (LabSIn) University of Campinas - UNICAMP Campinas, Campinas, Brazil

² Federal University of Technology – Paraná (UTFPR), Ponta Grossa, Brazil

The most common types of HESS are composed of batteries and ultracapacitors [10], seeking to combine the advantages from different power sources [13]. The high-energy-density of batteries provides vehicle autonomy and supports slow transients. In the meantime, the high-power density of the ultracapacitors can help the batteries to prolong their lifetime, which is susceptible to high-duty fluctuated currents [14] and also can recover energy from the regenerative braking. Moreover, the battery/ultracapacitors HESS enables battery size reduction, decreasing its cost, and also enhancing its power management. In EVs applications, it is not possible for the system to be powered only by ultracapacitors because the energy density is low and the price of an ultracapacitors bank is high [15].

Notwithstanding, the HESS practical performance is significantly influenced by its complex sizing and the power management strategy [16]. The HESS sizing challenge is to find the appropriate combination of ultracapacitor banks and battery cells to minimize costs and mass of the HESS and also maximize the battery's expected life cycle. Some studies have been done into optimal HESS sizing [17–20]. In most cases, the optimization constraints are transient power requirements, whereas cost, system efficiency, or fuel economy are usually selected as optimization objectives [21].

In power management control (PMC), rule-based strategies and optimization-based approaches are widely used [22, 23]. The first is normally created according to the engineering experience, heuristics, intuition, or mathematical models [16]. The second approach is classified as real-time and global optimizations. This last is composed for the neural network [24], dynamic programming [25, 26], convex programming [27], and other multi-objective optimization [6, 17, 28].

Most of the papers presented in the literature study the sizing and power management challenges separately [29], however, with this approach, only sub-optimal solutions are obtained [16]. Therefore, it is not possible to obtain the global optimal performance once the design and control problems of a HESS are coupled in practice [30]. In this way, this work will investigate the sizing, and the power management of the HESS, which will be also used as design variables to be optimized.

Regarding the vehicle topology, Shi et al. [31] and Liu et al. [32] highlighted the advantages of distributed electric propelling systems, with multiple actuators, concerning vehicle stability performance. Moreover, Othaganont et al. [7] optimized the drivetrain configurations considering four different EMs distribution; single EM assemble to a final drive system at the frontal wheels; two in-wheel EMs connected directly to the frontal wheels; and the replication of these previously described typologies coupled to both, frontal and rear propelling systems. Holjevac et al. [6] also showed the EMs associated with differential transmission

assembled to the frontal and rear axles. Furthermore, Eckert et al. [19] and Li et al. [33] studied improved EMs and HESS configurations for the four in-wheel drive EV. Beyond that, Corrêa et al. [34] and Eckert et al. [20, 35] also studied some of the listed configurations and added two extra alternatives that mixed the in-wheel and differential EMs assembly (Fig. 1), resulting in a better trade-off between battery size and driving range. However, all the mentioned EV configurations were analyzed only when submitted to standard driving cycles as the NEDC, WLTP, FTP-75, HWFET, and US06.

As mentioned before, previous studies used standard driving cycles that may generate solutions that are not optimal when applied to real driving conditions. On the other hand, the urban driving cycles are more complex, due to the frequent vehicle acceleration followed by deceleration [33], and are directly associated with the vehicle energy economy [36]. Therefore, this paper focuses on reaching an EV optimized for a real urban driving scenario, by simulating an experimentally obtained driving cycle of Campinas [37], one of the most populous cities of São Paulo State - Brazil. In addition, this cycle considers the road altimetry, a very important feature that influences the downhill regenerative braking and the uphill requested EMs traction power, frequently not considered in driving cycle standards.

The EV configuration used in this work is powered by an EM connected to a differential transmission system, which drives the rear wheels, and by two in-wheel electric motors (EMs) coupled directly to the front wheels, as shown in Fig. 1. The split of the power demand between the drive systems and the control of the power source which fulfills the EMs is done by the HESS power management control (PMC). The HESS analyzed considers a battery pack associated with an ultracapacitor.

In this way, the main purpose of this work is to optimize the mentioned EV configuration (Fig. 1) drivetrain and HESS size, by means of a bi-criteria optimization problem that minimizes the total mass of the HESS (battery + capacitors) and maximizes the EV driving range, under a real urban driving cycle. Thereby, a genetic algorithm (GA) was used considering the following design variables: battery

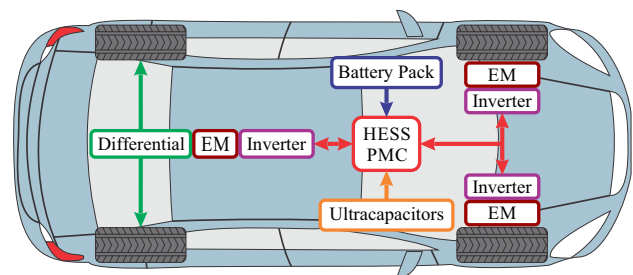


Fig. 1 Electric vehicle configuration

voltage, battery capacity, ultracapacitors model, ultracapacitors arrangement, EMs torque curves, differential transmission ratio, and the power split (between the HESS battery and capacitors) control parameter. The robust rule-based PMC was applied [35] to find the best efficiency trade-off between the propelling systems while minimizes the HESS discharges.

Finally, the Pareto frontier of non-dominated solutions defines the optimum EV configurations, in which the minimum HESS mass and the maximum drive range configurations were analyzed, in the same way as the solution that presents the best trade-off regarding the optimized criteria.

2 Simulation parameters

The analysis made considers the vehicle longitudinal dynamics modeled by the movement resistance forces, using the equations presented by Gillespie [38], associated with the maximum transmissible traction force [39], initially implemented to conventional vehicles [40, 41], and adapted to be applied on an EV in the current work.

One of the major movement resistance forces, mainly at low speed, is the rolling resistance (R_x) [N], caused by the tire deformation and adhesion on the contact area. It is a function of the vehicle speed (V) [m/s], mass (M) [kg], gravity acceleration (g) [m/s²] and road angle (α) [rad], described by Eq. (1).

$$R_x = 0.01 \left(1 + \frac{2.24 V}{100} \right) Mg \cos \alpha \quad (1)$$

Another load is the air resistance, represented by the aerodynamic drag (D_A) [N]. It is determined by Eq. (2) and depends on the air density (ρ) [kg/m³], on the vehicle speed (V) [m/s] and on the vehicle geometry (drag coefficient (C_D) and frontal area (A) [m²]).

$$D_A = \frac{1}{2} \rho V^2 C_D A \quad (2)$$

The total requested torque (T_{req}) [Nm] is based on the movement resistance forces (R_x and D_A), on the tire external radius (r) [m] and on the vehicle required acceleration (a_{req}) [m/s²], as shown in Eq. (3).

$$T_{\text{req}} = (M(a_{\text{req}} + g \sin \alpha) + R_x + D_A) r \quad (3)$$

As seen previously in Fig. 1, there are two different propelling systems at the wheels and their inertias need to be considered. Firstly, the inertia of the in-wheel EMs is added to the inertia of the frontal wheels (I_{wf}) [kgm²], once the EM is directly connected without any transmission system. Secondly, at the rear propelling system, the inertia of the motor

is added to the inertia of the differential (I_d) [kgm²], once it is connected to a differential and its transmission ratio (N_d).

For the first case, the requested torque (T_{req}) defined by Eq. (3) is divided by the PMC between the propelling systems, frontal and rear. The frontal torque required T_{reqF} [Nm] is split to each one of the two EMs (T_{EMF}) and the frontal wheels' inertia with the coupled motors (I_{wf}) [kgm²] is also considered, as determined by Eq. (4).

$$T_{\text{EMF}} = \frac{T_{\text{reqF}} + I_{\text{wf}} \frac{a_{\text{req}}}{r}}{2} \quad (4)$$

For the second case, the rear EM torque (T_{EMR}) [Nm], as shown in Eq. (5), is defined as a function of the required torque T_{reqR} [Nm] and the inertias divided by the efficiency (η_d) and by the differential transmission ratio (N_d). The inertia terms in Eq. (5) include the differential with its coupled EM in I_d and the two rear wheels inertia I_{wr} [kgm²].

$$T_{\text{EMR}} = \frac{T_{\text{reqR}} + (I_d N_d^2 + I_{\text{wr}}) \frac{a_{\text{req}}}{r}}{N_d \eta_d} \quad (5)$$

However, the motors required torques (T_{EMF} and T_{EMR}) are limited by the available EMs propelling torques and also by transmissible torque limit on the tire-ground contact [42, 43]. The T_{AF} [Nm] and T_{AR} [Nm] (maximum EM available torques) are determined by the maximum torque curves according to the motors' speed, as seen in the electric motors model section. The other limiter is the maximum transmissible torque $T_{R(\text{max})}$ or $T_{F(\text{max})}$ defined in Eqs. (6) and (7), as explained by Jazar [39]. Therefore, the PMC has to prevent traction limit excesses in the propel systems requiring less torque than the indicated limits.

$$T_{R(\text{max})} = \mu \left(\frac{Mg \cos \alpha b + h \sin \alpha + Mh a_x}{2L} \right) r \quad (6)$$

$$T_{F(\text{max})} = \mu \left(\frac{Mg \cos \alpha c - h \sin \alpha - Mh a_x}{2L} \right) r \quad (7)$$

In Eqs. (6 and 7), μ is the friction coefficient on the tire-ground contact. Moreover, the vehicle acceleration is considered equal to the required acceleration as an initial approximation ($a_x = a_{\text{req}}$). Geometrical parameters were also used, such as the vehicle wheelbase (L) [m], gravity center height (h), [m] and its longitudinal distance between the vehicle rear (c) [m] and frontal (b) [m] axes.

Whether the requested motor torques T_{EMF} and/or T_{EMR} exceed the mentioned limits, the performance will be bounded by the lower torque value of each driving system. The traction front T_F (Nm) and rear T_R (Nm) torques to propel the vehicle are shown in Eqs. (8 and 9).

$$T_F = \min \begin{cases} 2T_{EMF} - I_{wf} \frac{a_x}{r} \\ 2T_{AF} - I_{wf} \frac{a_x}{r} \\ T_{F(max)} \end{cases} \quad (8)$$

$$T_R = \min \begin{cases} T_{EMR}N_d\eta_d - (I_dN_d^2 + I_{wr}) \frac{a_x}{r} \\ T_{AR}N_d\eta_d - (I_dN_d^2 + I_{wr}) \frac{a_x}{r} \\ T_{R(max)} \end{cases} \quad (9)$$

According to the second Newton’s law, resultant acceleration is a relation between the sum of the forces and the mass in the movement, in this case, the vehicle mass. Thus, the resultant vehicle acceleration a_x [m/s²] is defined as indicated by Eq. (10).

$$a_x = \frac{\frac{T_F+T_R}{r} - D_A - R_x - Mg \sin(\alpha)}{M} \quad (10)$$

The maximum transmissible torques presented in Eqs. (6 and 7) change with the resultant acceleration value a_x , featuring an iterative process from Eq. (7, 8, 9 and 10). This process is performed until the a_x convergence. Once the real acceleration is known, the vehicle speed V [m/s] is obtained integrating the a_x value, finishing the simulation loop. The vehicle parameters used in the simulation are shown in Table 1.

Since the values of traction and acceleration have converged, the effective frontal and rear EMs torques (T_{Fef} [Nm] and T_{Ref} [Nm]) are calculated by Eqs. (11 and 12).

$$T_{Fef} = \frac{T_F + I_{wf} \frac{a_x}{r}}{2} \quad (11)$$

$$T_{Ref} = \frac{T_R + (I_dN_d^2 + I_{wr}) \frac{a_x}{r}}{N_d\eta_d} \quad (12)$$

2.1 Electric motors model

The optimization defines the EMs speed and torque values as parameters. Figure 2 presents a generic torque curve and efficiency map, based on the studies of Eckert et al. [19, 20, 35]. This approach is a simplified way to find optimum configurations for the EMs, once a theoretical torque curve is generated and the efficiency map is interpolated according to it. This enables a significant reduction in the computational cost of the model.

There are four main points in Fig. 2. The first one is when the EM torque is maximum (T_{max}) [Nm] at null speed, representing the startup torque. The second one is the torque constant phase, with the same T_{max} value of the previous point, and its respective speed (ω_{Tc} [rad/s]). Tong [45] shows that the best operating point of the EM happens between $0.1T_{max}$ and $0.3T_{max}$ at the constant power regime. Therefore, the third point T_{pc} [Nm] is determined as the recommended upper limit (30% T_{max}) [8, 20], in Eq. (13). Knowing the EM power is constant, speed values ω_{pc} [rad/s] are defined according to Eq. (14).

$$T_{pc} = 0.3T_{max} \quad (13)$$

Table 1 Simulated vehicle parameters [35, 44]

Vehicle mass without HESS (M_{wh})	800 kg
Tires 175/70 R13 radius (r)	0.2876 m
Wheels + tires inertia (I_w)	2 kgm ²
Tire peak friction coefficient (μ)	0.9
Vehicle frontal area (A)	1.8 m ²
Drag coefficient (C_D)	0.33
Differential transmission ratio (N_d)	4.87
Differential inertia (I_d)	9.22E-04 kgm ²
Differential efficiency (η_{td})	0.9
Wheelbase (L)	2.443 m
Gravity center height (h)	0.53 m
Front axle to gravity center (b)	0.983 m
Rear axle to gravity center (c)	1.460 m
5 kW EM inertia	0.1 kgm ²
12 kW EM inertia	0.2 kgm ²
30 kW EM inertia	0.3 kgm ²

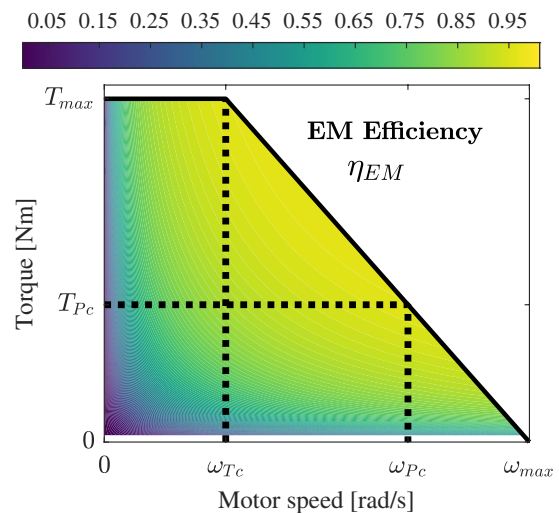


Fig. 2 Electric motor efficiency map [19, 35]

Table 2 Inverter efficiency map [35, 46]

T_{EM}	ω_{EM}				
	$0.1\omega_{Pc}$	$0.3\omega_{Pc}$	$0.5\omega_{Pc}$	$0.7\omega_{Pc}$	ω_{Pc}
0	0.65	0.84	0.9	0.84	0.83
$0.11T_{max}$	0.74	0.89	0.94	0.91	0.91
$0.33T_{max}$	0.82	0.93	0.96	0.96	0.96
$0.56T_{max}$	0.83	0.94	0.97	0.97	0.97
T_{max}	0.83	0.94	0.97	0.97	0.97

$$\omega_{Pc} = \frac{T_{max}\omega_{Tc}}{T_{Pc}} \tag{14}$$

The last important point is defined as the zero torque and the EM maximum speed (ω_{max} rad/s) and it is calculated using a linear extrapolation based on the previous points, (T_{max} , ω_{Tc}) and (T_{Pc} , ω_{Pc}).

Lastly, based on the interpolation of the points (T_{max} , ω_{Tc}) and (T_{Pc} , ω_{Pc}), the curves that determine the available torques (T_{AF} and T_{AR}) are defined. Once the torque curves are defined, the respective EM efficiency maps (η_{EMF} and η_{EMR}) are obtained. Moreover, the EMs inertias are interpolated based on the values presented in Table 1.

After the definitions of motors efficiencies (η_{EMF} and η_{EMR}) and their respective inverse efficiencies (η_{invF} and η_{invR}), according to Table 2, the total electrical current consumption I [A] of the vehicle is determined as shown in Eq. (15). Beyond efficiencies, it is a function of the HESS voltage V_{HESS} (V), of the current EM speed ω_{EM} (rad/s), and of the EM effective torques T_{Fef} and T_{Ref} .

$$I = \frac{2T_{Fef}V}{r V_{HESS} \eta_{EMF} \eta_{invF}} + \frac{T_{Ref}VN_d}{r V_{HESS} \eta_{EMR} \eta_{invR}} \tag{15}$$

Over than providing power during accelerations, the EMs can retrieve part of the kinetic energy during the braking, acting as generators [47] to recharge the HESS ultracapacitors. This braking energy recovery represents an effective approach to increase the EV driving range [48]. In this study, the regenerative braking capacity is bounded to 10% of its maximum torque [19]. Whenever the required torque to brake exceeds this limit, the residual one is supplied by the vehicle’s frictional brake system [49].

2.2 Ultracapacitor and battery models

The PMC divides the current I (A) between the HESS power sources (as seen in Eq. (15)), in this case, a battery pack and an ultracapacitor.

One of the main objectives of this study is to find out the optimum battery size for the EV HESS, therefore, a simplified method is applied to estimate the battery mass

M_{bat} (kg) as seen in Eq. (16). Once the capacity B_c (Ah) and the battery voltage V_{bat} [V] will be determined by the optimization algorithm (see Sect. 4), the M_{bat} is defined by lithium-ion specific energy S_E . The battery considered is a lithium-ion model (Simulink™database).

$$M_{bat} = \frac{V_{bat}B_c}{S_E} \tag{16}$$

In this paper, it is assumed the state-of-the-art lithium-ion batteries, considering $S_E = 150$ (Wh/kg) specific energy [50, 51]. This S_E value was also reported as typical for EV batteries [52, 53]. It is important to highlight that this simplified approach is used only to define the optimum battery capacity B_c and voltage V_{bat} by simulations. Once the optimum parameters were defined, it is necessary to design or to find out a commercial battery that these required parameters are able to be applied in the real HESS.

Knowing the specific battery power P_{max} (300 [W/kg] for lithium-ion batteries), the mass M_{bat} and the voltage V_{bat} values, the maximum discharge current I_{max} (A) of the battery is determined as indicated by Eq. (17).

$$I_{max} = \frac{P_{max}M_{bat}}{V_{bat}} \tag{17}$$

Another source is the ultracapacitor Cap. The ultracapacitors model can be simplified as ideal capacitors C_{uc} in series with their respective internal resistances R_{uc} where the parallel resistance was neglected as presented by Zhang and Mi [54]. The parameters used for the ultracapacitor simulations are presented in Table 3.

Table 3 Ultracapacitor parameters [19, 20]

Cap(<i>n</i>)	$V_{uc(n)}$ [V]	$C_{uc(n)}$ [F]	$R_{uc(n)}$ [Ω]	$M_{uc(n)}$ [kg]
Cap(1)	16	108	3.6E-03	3.0
Cap(2)		108	4.3E-03	3.7
Cap(3)		200	3.5E-03	4.1
Cap(4)		266	3.0E-03	4.6
Cap(5)		333	2.4E-03	5.1
Cap(6)		500	1.9E-03	6.0
Cap(7)	48	36	13E-03	9.5
Cap(8)		66	10.4E-03	11.5
Cap(9)		88	8.9E-03	12.5
Cap(10)		111	7.1E-03	13.5
Cap(11)		166	5.6E-03	16.0
Cap(12)	64	83	9.5E-03	17.0
Cap(13)		125	7.5E-03	20.0
Cap(14)	86	62	12.7E-03	21.0
Cap(15)		93	10E-03	26.0
Cap(16)	125	62	15E-03	67.0

Capacitors connected in parallel in the HESS present no vantage when compared to those connected in series, as asserted by prior works [19, 55]. Thus, the bank of ultracapacitors considered has only series arrangements and demand N_s units, quantified in Eq. (18).

$$N_s = \frac{V_{bat}}{V_{uc(n)}} \tag{18}$$

Once defined the quantity N_s , the total mass of the capacitors M_{cap} (kg) is worked out by Eq. (19).

$$M_{cap} = N_s M_{uc(n)} \tag{19}$$

Similar to the work of Ravey et al. [56], the previously calculated masses of the battery M_{bat} and the ultracapacitors M_{cap} are added to the EV mass without the HESS M_{wh} (kg) (seen Table 1) to define the total vehicle mass M as shown in Eq. 20.

$$M = M_{wh} + M_{bat} + M_{cap} \tag{20}$$

According to Yang et al. [57] and Prochazka et al. [58], deep discharging and over-charging of the Li-ion cells must be avoided to ensure sufficient lifetime. Therefore, to avoid damages provoked by the whole battery discharge, the power source charge condition SoC is limited by the vehicle PMC to 40% [34, 59]. For the same reasons, the capacitors discharge also is limited by the PMC [60].

2.3 Power management control model

The PMC controls the power using a rule-based strategy and considering the EMs/inverters efficiency in its algorithm. It uses a discretization loop to evaluate all possible propelling arrangements among the available drive systems and to distribute the EMs (frontal and rear) requested torque T_{req} , as shown in Eqs. (4 and 5). It is important to highlight it may exist some cases where the use of only one drive system is better than a combination of both.

This control splits the EV power demand in such a way that the battery supplied continuous power and the supercapacitor quickly compensates the instantaneous demands, acting as power buffers [61–63]. With all these features, the PMC keeps the EV working while it generates fewer HESS discharges, which is the best global efficiency among the EMs and its inverters. The PMC algorithm is shown in Fig. 3.

In order to avoid poor acceleration caused by excessive tire slipping, this control also considers the tire ground traction limit, according to Eqs. (7 and 6), which define the maximum applicable torques on the vehicle wheels. In this way, the traction limits will not be exceeded while the propelling systems fulfill the torque request.

It is well known that the major advantage of assembling batteries and ultracapacitors in a HESS is transferring the high peak powers response to the ultracapacitors, avoiding the battery high-frequency power fluctuations [64]. Ma et al.

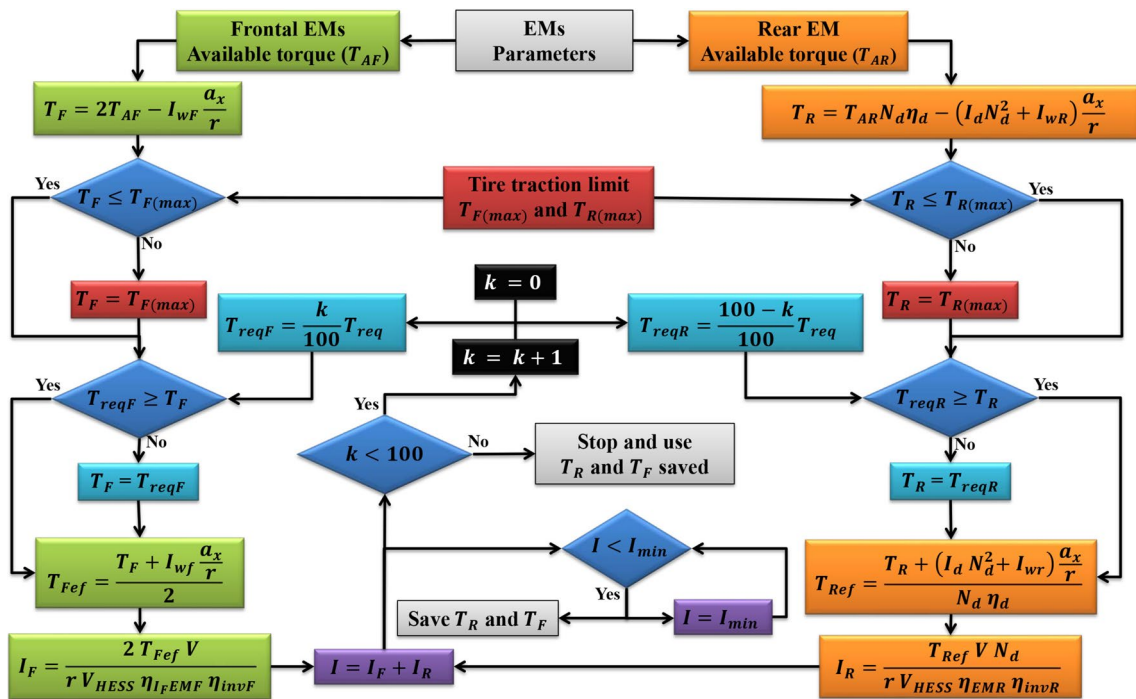


Fig. 3 Power management control algorithm

[61] highlight that the batteries are more efficient at low and steady power loads, therefore, to make these devices robust to current spikes, it is necessary to excessively increase their storage capacity. Furthermore, Veneri et al. [65] showed that high charging and discharging rates reduce battery efficiency because it is difficult for these devices to recover from rapid power fluctuations, which leads to a lifetime decrease [61]. On the other hand, the ultracapacitors are designed to provide high power and their life cycles are much longer than those presented by batteries [62].

In this paper, the maximum discharge current I_{max} of the battery is multiplied by a percentage P_1 (%) to define the battery current limit, which is defined by the optimization algorithm limit ($I_{lim} = P_1 I_{max}$ [A]). If the required current I (A) defined in Eq. (15) exceeds the battery current limit ($I > I_{lim}$), the ultracapacitors provide the remaining required current. In Eq. (21), it is shown the calculation of the battery I_{bat} (A) and ultracapacitors I_{cap} (A) currents. This current split strategy was previously implemented by Eckert et al. [19, 20] and Corrêa et al. [55], presenting satisfactory results.

$$\begin{cases} \text{if } I \leq I_{lim} ; I_{bat} = I \text{ and } I_{cap} = 0 \\ \text{if } I > I_{lim} ; I_{bat} = I_{lim} \text{ and } I_{cap} = I - I_{lim} \end{cases} \quad (21)$$

Such rule-based power split strategy where the battery provides the average required power and the ultracapacitors fulfill the peak power is presented by Veneri et al. [65]. Moreover, this strategy also considers the possibility of the battery providing the maximum capable discharge power and the ultracapacitors pack providing the remaining required power. Furthermore, when the power demand is very high, the battery can provide the power directly to the motors [63].

Because the discharge limit of the capacitors is higher than the battery limit, the required I_{cap} values are not limited. Therefore, the input current resulting from the regenerative braking is fully absorbed by the ultracapacitors, isolating the battery from these power peaks [62–64]. In the same way as the battery, the ultracapacitors pack is also limited to avoid its complete discharge, which decreases its life, thus, when the ultracapacitors stage of charge SoC_{UC} (%) is less than 35%, the EV will only be driven by the battery, limited to its I_{lim} value. Therefore, the vehicle will exhibit a decrease in acceleration performance due to the reduced torque EMs.

2.4 Driving cycle

In the analysis made in this paper, the simulations were developed with an experimental driving cycle proposed by Oliveira et al. [37]. This cycle allows us to evaluate the EV performance based on the urban driving reality from Campinas city (Fig. 4). Moreover, this cycle was successfully applied in the optimization process of a hybrid

vehicle drivetrain [66]. The driving cycle profile, shown in Fig. 4ab, provides the target speed V_t (m/s), that is compared to the actual EV speed V (m/s) to define the requested acceleration calculation a_{req} , as seen in Eq. (22). The V_t is the speed one-time step Δ_t (s) ahead of the current simulation time. Furthermore, Fig. 4c provides data to define the road angle α from the cycle’s altimetry. The real-world driving cycle has a duration of 7500 s and 42 km, normally a reality of Brazilian traffic in some cities.

$$a_{req} = \frac{V_t - V}{\Delta_t} \quad (22)$$

3 Optimization algorithm

The optimization uses a GA technique to minimize the total mass of the HESS (battery + ultracapacitors), that corresponds to the first optimization criterion f_1 , as seen in Eq. (23). The second criterion f_2 (Eq. (24)) is to maximize the EV drive range (DR), represented by the traveled distance reached by the EV when the battery reaches the maximum allowed discharge limit ($SoC = 40\%$), considering the repetition of the analyzed driving cycle. The optimization algorithm is implemented in MATLAB™.

$$f_1 = \min(M_{bat} + M_{cap}) \quad (23)$$

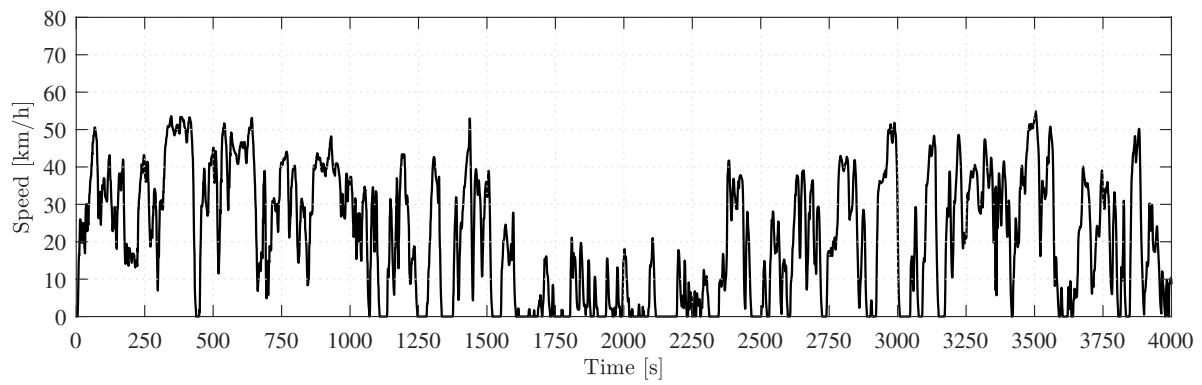
$$f_2 = \max(DR) \quad (24)$$

The GA technique requires the definition of a chromosome $[X]$, which has the optimization parameters used at the EV simulation. Several of these chromosomes and their data make a population database. This algorithm defines the battery voltage V_{bat} (V) and capacity B_C (Ah), to optimize the criteria presented in Eq. (23) and Eq. (24) (f_1 and f_2). With this information, the algorithm allows obtaining the battery mass M_{bat} using Eq. (16). The GA also decides the ultracapacitor type n that will be used among the available presented in Tab. 3 and the series capacitors number is obtained by Eq. (18).

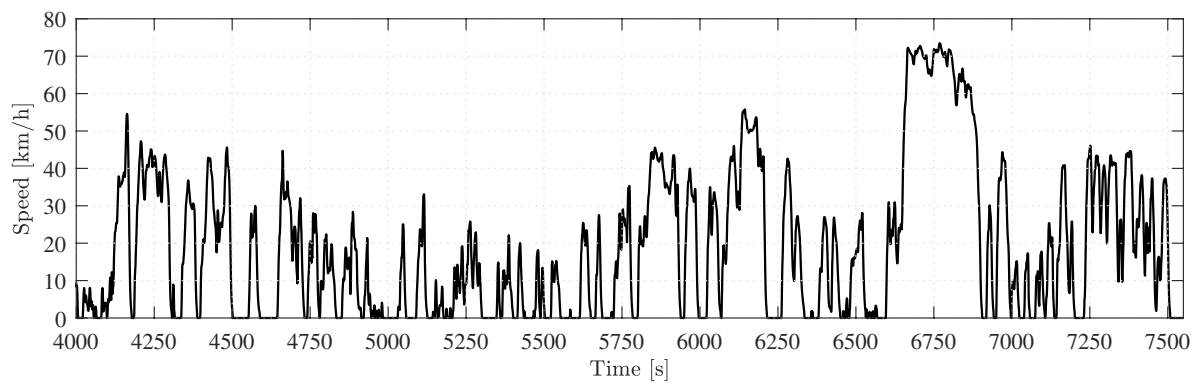
Another important parameter in the chromosome is the maximum current percentage of the battery P_1 (%). It is needed to determine the current limit I_{lim} of the battery that is used by the power control to split the current between the ultracapacitors and the battery of the HESS. The chromosome $[X]$ with the optimization criteria is shown in Eq. (25).

$$[X] = [V_{bat} \ B_C \ n \ T_{maxF} \ \omega_{TeF} \ T_{maxR} \ \omega_{TeR} \ N_d \ P_1] \quad (25)$$

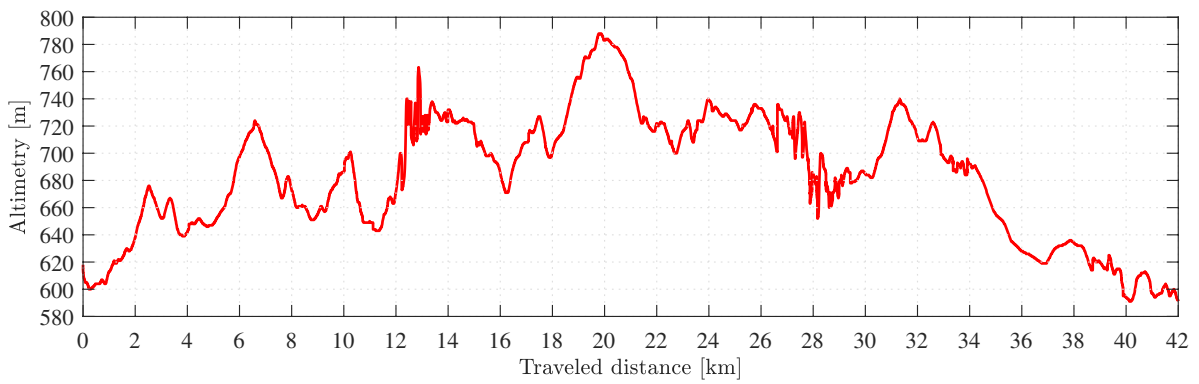
Subject to: constraints C presented in Eq. (26).



(a) Speed profile part 1



(b) Speed profile part 2



(c) Altimetry profile

Fig. 4 Campinas driving cycle [37]

$$C(\mathbf{X}) = \begin{cases} 100 \leq V_{bat} \leq 400 & (\text{V}) \\ 50 \leq B_C \leq 150 & (\text{Ah}) \\ 1 \leq n \leq 16 \\ 50 \leq T_{maxF} \leq 300 & (\text{Nm}) \\ 250 \leq \omega_{TcF} \leq 3000 & (\text{rpm}) \\ 10 \leq T_{maxR} \leq 50 & (\text{Nm}) \\ 500 \leq \omega_{TcR} \leq 1500 & (\text{rpm}) \\ 3.5 \leq N_d \leq 7 \\ 5 \leq P_1 \leq 95 & (\%) \end{cases} \quad (26)$$

To ensure the EV can execute the proposed driving cycle, the vehicle performance acts as a constraint. Therefore, the simulated solutions need to present a minimum traveled distance of 98% of the standard Campinas driving cycle (42.11 km in its first repetition) or they are removed from the population. Furthermore, it is required the EV performs at least two complete loops of the driving cycle (DR ≈ 82.52 km, considering the minimum acceptable performance) to include its solution in the population.

3.1 Selection, Crossover and Mutation

The Pareto ranking classifies the population using the adaptive-weight approach [67] for fitness values. For the non-dominated solutions, the Pareto frontier receives the first rank $P = 1$. Based on the dominated solutions only from the first rank solutions, it is determined the second rank $P = 2$, and so on. For the first Pareto frontier rank ($P = 1$), the $P_R = 1$, increasing its fitness value. On the other hand, the dominated solutions ($P \geq 2$) receive $P_R = 0$.

The fitness formulation also considers the optimization criteria. For each optimization criterion j , the maximum $f_{j_{pop}^{max}}$ and minimum $f_{j_{pop}^{min}}$ values are defined. As shown in Eq. (27), $f_{j_{pop}^{max}}$ and $f_{j_{pop}^{min}}$ are used to calculate a weight value $f_j(\mathbf{X})$ for each solution.

$$Ft(\mathbf{X}) = \frac{f_{1_{pop}^{max}} - f_1(\mathbf{X})}{f_{1_{pop}^{max}} - f_{1_{pop}^{min}}} + \frac{f_2(\mathbf{X}) - f_{2_{pop}^{min}}}{f_{2_{pop}^{max}} - f_{2_{pop}^{min}}} + P_R \quad (27)$$

The roulette wheel method was chosen for the algorithm selection procedure, aiming to raise the probability of higher fitness $Ft(\mathbf{X})$ values in the selected members. As seen in Eq. (28), this probability $S_p(\mathbf{X})$ is defined based on the sum of the fitness values $Ft(\mathbf{X})$ of every member ($1 \leq k \leq P_s$), where P_s is the size of the population.

$$S_p(\mathbf{X}) = \frac{Ft(\mathbf{X})}{\sum_{k=1}^{k=P_s} Ft(\mathbf{X}_k)} \quad (28)$$

Based on the $S_p(\mathbf{X})$, the crossover operator chooses five pairs of population members $[\mathbf{X}]$ from the database. The new chromosome $[\mathbf{X}]$ generated is a random combination, with

Table 4 Mutation operator

Mutation operator	Mutated Chromosome $[\mathbf{X}_{Mi}]^T$
$MUT \geq 0.5$	
$-50 \leq V_{mut} \leq 50$	$V_{bat} + V_{mut}$
$-20 \leq B_{mut} \leq 20$	$B_C + B_{mut}$
Integer value ($1 \leq n_{mut} \leq 16$)	n_{mut}
$-5 \leq T_{mut} \leq 5$	$T_{max} + T_{mut}$
$-500 \leq \omega_{mut} \leq 500$	$\omega_{Tc} + \omega_{mut}$
$-1 \leq N_{mut} \leq 1$	$N_d + N_{mut}$
$5 \leq P_{mut} \leq 95$	P_{mut}

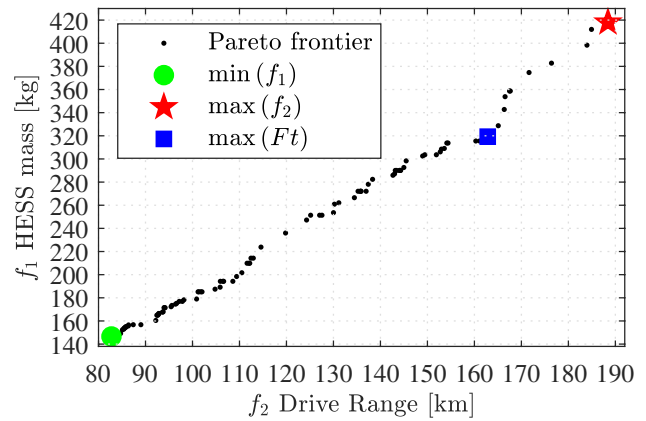


Fig. 5 Optimization results

equal probability among the selected, of the design variables of each selected pair of solutions [68]. A new simulation is made with this new chromosome $[\mathbf{X}]$ and the result is included in the population. This crossover procedure is replicated in the optimization until one of the parameters, at least, differs from the selected member, in order to avoid a configuration already simulated.

A simple way of mutation in the case of binary representation is just flipping the chromosomes' value. The mutation operator modifies some of the parameters from the selected pair of solutions and also from the chromosome generated by the crossover process. In this way, new values are inserted into the population. The mutation operator generates a random value ($0 \geq MUT \geq 1$) to define whether the selected parameter will or not be mutated. For each parameter, the probability of mutation is 50%.

The constraints $[C]$ in Eq. (26) must be considered by the mutated parameters. If one of the parameters exceeds the limits of the constraints or if no parameters of the chromosome generated present mutation, then this chromosome is disregarded and a new mutation is made until generating a combination that considers the constraints $[C]$. Table 4 shows the mutation limits.

The first population has 100 simulation results that respect the constraint limits. Each one of these was obtained by randomly defined chromosomes. The maximum population size was established as $P_{lim} = 500$. When the population oversteps the limit, the last Pareto rank (worst results) is deleted from the population. Whether the non-dominated solutions ($P = 1$) overstep the population limit, it is redefined as $P_{lim} = P_{lim} + 100$.

The convergence criterion is defined by the recurrence of the same Pareto frontier [69] for over 10 generations. Each generation is defined by the offspring of five-pairs of selected chromosomes combined with the crossover and mutation operators.

4 Results

The GA algorithm convergence results in a set of non-dominated solutions (Pareto frontier) presented in Fig. 5. These EV configurations are considered as optimum compromised solutions with a trade-off between the two optimization criteria. Among these results, three were selected to be analyzed in this section. The first one is the $\min(f_1)$ solution that corresponds to the minimum mass of the HESS system. The second one is the $\max(f_2)$ that improves the estimated drive range of the EV and the last one is the solution that presents the best trade-off between the optimization criteria, in other words, the solution that has the higher fitness value among the optimum configurations $\max(Ft)$.

Table 5 presents the design variables and respective results of the three selected configurations: $\min(f_1)$, $\max(f_2)$ and $\max(Ft)$.

Due to the uniformity of the analyzed driving cycle, it is composed basically of urban driving behavior (lowes speed and acceleration) and it only presents a small section of high speed (250 s at ≈ 70 km/h). The optimum EV configurations do not present a large variation as shown in Tab. 6, especially in the drivetrain design variables, that were minimized according to the HESS additional mass.

The optimum HESS configurations converge to the use of the capacitor $n = 1$ and $n = 8$. The variation in the battery design variables (V_{bat} and B_c) associated with the percentage

Table 6 Limit values of the optimum solutions chromosomes

Optimum solutions	Minimum value	Maximum value	Mean value	Standard deviation
V_{bat} (V)	104.63	295.15	181.52	60.84
B_c (Ah)	103.25	149.89	136.04	12.97
n	1	8	---	---
T_{maxF} (Nm)	133.42	230.29	180.25	22.08
ω_{TcF} (rpm)	255.03	316.71	264.06	9.65
T_{maxR} (Nm)	13.44	49.56	31.94	9.78
ω_{TcR} (rpm)	552	1380	1000	176.50
N_d	4.04	6.99	6.23	0.66
P_I (%)	5.42	92.70	38.09	26.77

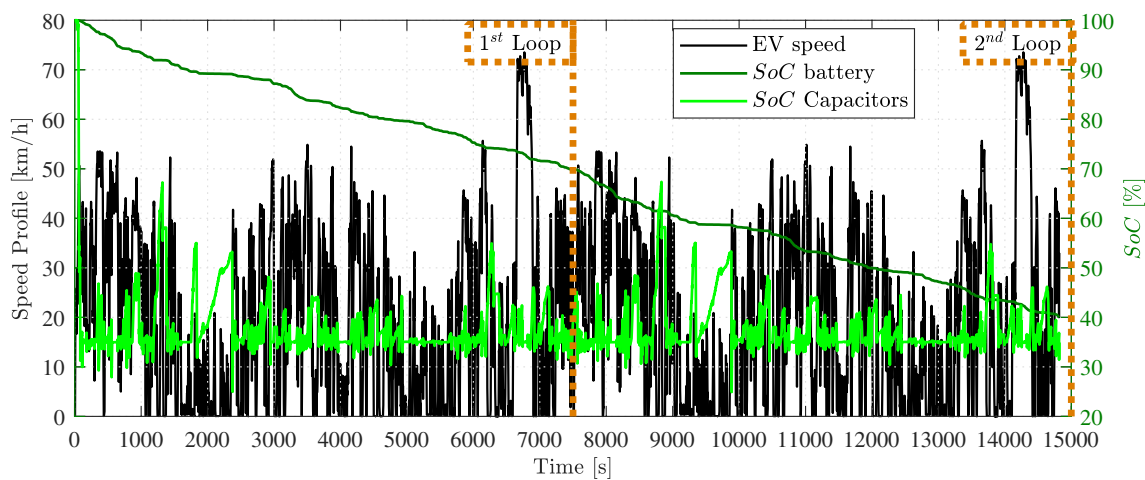
P_I , that controls the HESS power split, defines the estimated drive range of the EV that vary from 82.75 km (minimum acceptable drive range of 2 cycle loops) up to 188.43 km (largest HESS pack). The EV power system and resulting speed profile for the three selected configurations are presented in Fig. 6.

As presented in Fig. 6, the HESS capacitor state of charge SoC_{UCi} behavior is very similar in the three analyzed cases. Because the optimum capacitors (Cap(1), Cap(2) and even Cap(7)) models do not assemble a high power pack, the SoC_{UCi} drops at the beginning of the cycle until it reaches the maximum allowed discharge of 35%. On the other hand, this low power capacity ultracapacitor pack enables faster recharging during regenerative braking, which is amplified in the downhill sections, as presented in Fig. 7. Also, it shows the SoC_{UCi} of the three analyzed solutions. In other words, a low-power ultracapacitors pack presents a fast discharge while performs a quick recovery, ensuring the system will be able to assist the battery in the current demand peaks. This SoC_{UCi} charging/discharging behavior is repeated during the remaining driving time.

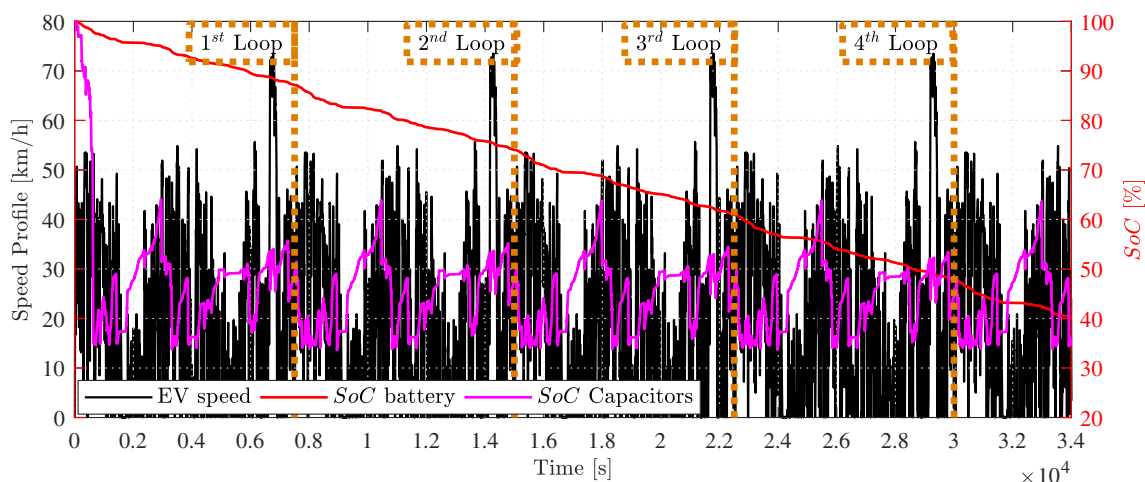
Besides the HESS system similar behavior of all analyzed solutions, the best trade-off ($\max(Ft)$) configuration presents a driving range close to the $\max(f_2)$ solution (25.6 km or 13.58%), however, with HESS pack 23.63% lighter (less 98.78 kg). This happens basically because the HESS mass increases the EV total mass M and, consequently, it increases

Table 5 Non-dominated solution

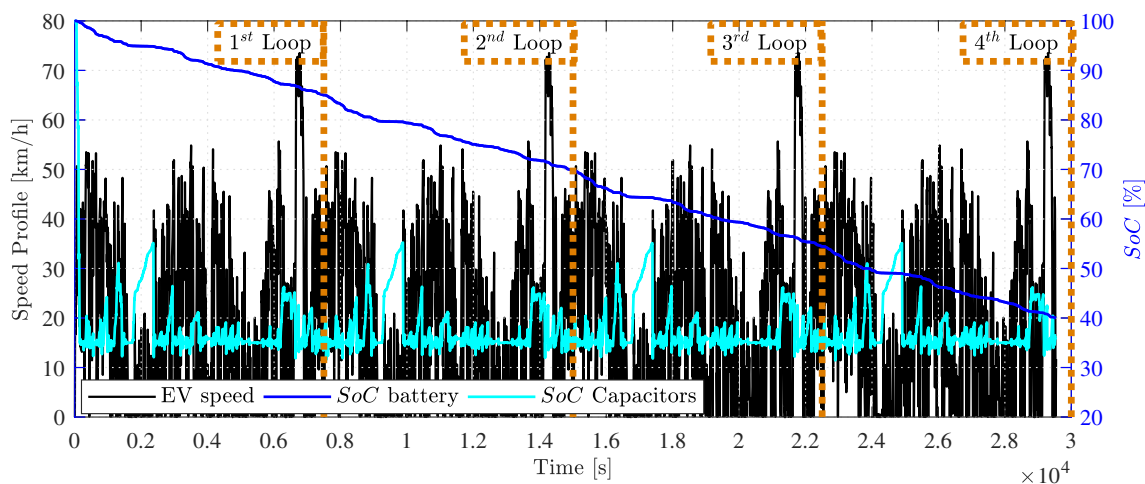
Solutions	Frontal drive		Rear drive			Capacitor			Battery				HESS mass (kg)	Drive range (km)	Fitness
	T_{maxF}	ω_{TcF}	T_{maxR}	ω_{TcR}	N_d	n	N_s	M_{cap}	V_{bat}	B_c	P_I	M_{bat}			
	(Nm)	(rpm)	(Nm)	(rpm)				(kg)	(v)	(Ah)	(%)	(kg)			
$\min(f_1)$	201.90	263	41.86	795	5.64	1	7	21	108	139	8.18	83.62	146.58	82.75	2.00
$\max(f_2)$	199.72	263	22.82	1210	6.1	2	19	70.30	295	141	12.80	347.72	418.02	188.43	2.00
$\max(Ft)$	171.23	263	25.78	1097	6.74	7	5	42.50	239	139	6.55	276.74	319.24	162.83	2.12



(a) $\min(f_1)$ Minimum HESS mass



(b) $\max(f_2)$ Maximum stimulated drive range



(c) $\max(Ft)$ Best trade-off

Fig. 6 HESS state of charge behavior and resultant speed profile according to the optimized EV configurations

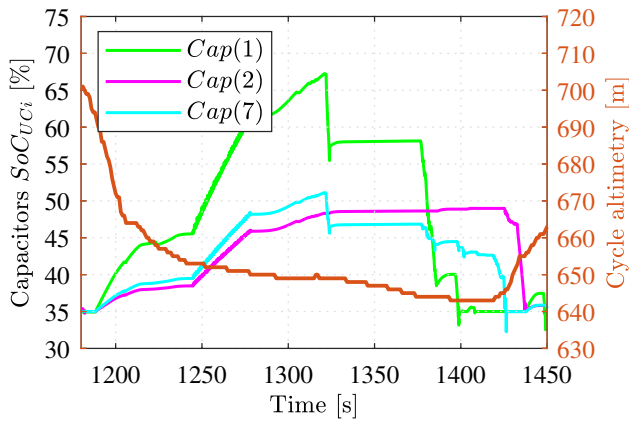


Fig. 7 Capacitors SoC_{Uci} during a downhill section of the cycle

the vehicle power demand, as shown in Eqs. (1 and 3). In other words, even with more power capacity, a bigger HESS also implies a power consumption increase that limits the HESS size. Furthermore, the bigger HESS system implies technical difficulties to assemble all components in the vehicle.

On the other hand, smaller HESS, as the min (f_1), presents 54.08% less mass as compared to the max (Ft) configuration, however, the driving range also decreases 49.18%. This specific configuration can be applied in smaller EVs developed for short travels or cities with available charging parks in the EV drive range.

Regarding the EVs drivetrain, it was possible to conclude the resulting configurations are most indicated to urban driving, due to the optimization constraints and mostly because of the chosen driving cycle. The major limitation of this configuration is related to the maximum vehicle speed, once the EMs reach null torque in a specific rotation, that is a direct function of the vehicle longitudinal speed, according to the drive train configuration (in-wheel or differential system).

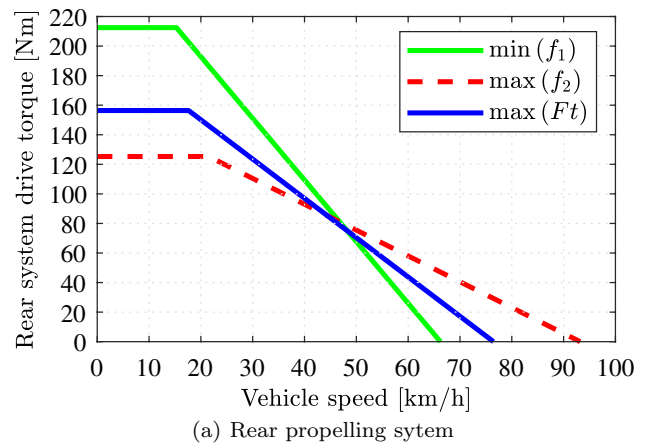
Equations (29 and 30) show the correlation between the EMs and vehicle speed for the frontal V_{Front} (m/s) and rear V_{Rear} (m/s) driving systems, respectively. The resulting torque curve for the frontal T_{Front} [Nm] and rear T_{Rear} (Nm) propelling systems are presented by Eqs. (31 and 32).

$$V_{Front} = \frac{\pi r \omega_{EMF}}{30} \tag{29}$$

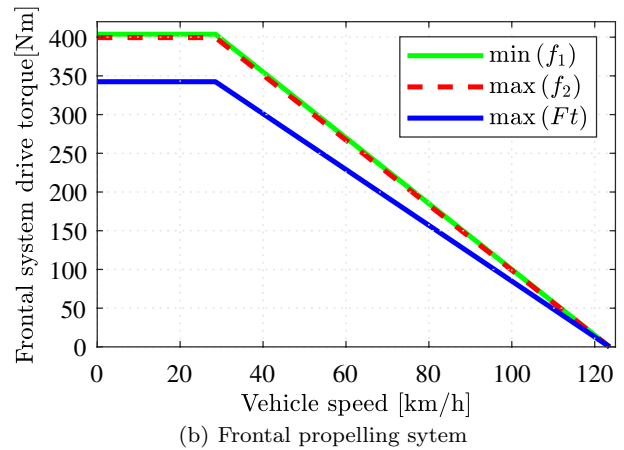
$$V_{Rear} = \frac{\pi r \omega_{EMR}}{30 N_d} \tag{30}$$

$$T_{Front} = 2T_{EMF} \tag{31}$$

$$T_{Rear} = T_{EMR} N_d \eta_d \tag{32}$$



(a) Rear propelling system



(b) Frontal propelling system

Fig. 8 Rear and frontal effective traction torque (at wheels) according to the vehicle speed for the optimum EV configurations

The resulting torque curves as a function of the vehicle speed and drivetrain configurations are presented in Fig. 8 and it is possible to observe the rear system reaches null torque up to 60 km/h (min (f_1) solution) and up to ≈ 92 km/h (min (f_2) solution). This happens because the differential gear transmission ratio increases the system's final torque and also allows it to quickly reaches the good efficiency region of the EM (see Fig. 2). This kind of assembling is useful in urban driving, where the vehicle needs to stop several times, especially in jammed traffic conditions as presented between the 1600 and 2300 s (Fig. 4a) and between 5100 and 5600 s (Fig. 4b) of the analyzed cycle.

However, this kind of assembly presents some additional issues. Besides the low-speed limit, this EM needs to be disconnected when it reaches critical speed, possibly by the addition of a clutch system in the powertrain, avoiding possible EM damages caused by high rotation. On the other hand, the rear EM operation at higher rotations could improve the regenerative braking efficiency, but it is necessary to carefully evaluate it due to the EMs operation speed limit.

Once the rear propelling system optimization leads to improve the EV startup and low-speed performance, the frontal in-wheel EMs become responsible to propel the vehicle in the renaming situations, fulfilling the torque demand at low speed and also acting as a single propelling system when the EV reaches the speed of null torque in the rear system.

Finally, the resulting EMs become capable to fulfill the power demand, without significant performance losses, once these configurations were able to complete the desired speed profile. However, the optimization process minimizes the EMs, because smaller EMs reach the high-efficiency regions faster than the larger ones and it results in frontal EMs that reach null torque at ≈ 125 km/h. In this situation, the rear propelling system is already disabled. However, in these high-speed situations, the EV power demand increases especially by the aerodynamic drag action and it can overcome the available traction power, provided only by the frontal in-wheel EMs. Therefore, it may represent an issue, if this vehicle needs to be used in an overtaking and/or highway situation, where high speeds are required.

5 Conclusion

This paper showed a simulation-based approach to the sizing of an EV battery/ultracapacitor pack and drivetrain, using a real driving cycle recorded in Campinas City. A comparative analysis of the EV optimizations was made, considering three different solutions: the maximum drive range, the minimum HESS mass and the best combination between these criteria. The optimization results show that the HESS system presents a similar behavior in all analyzed solutions. Moreover, the optimum EMs converge to a minimum size that reaches the higher efficiency regions faster, without compromising the vehicle acceleration performance.

Furthermore, the results show that HESS technology currently provides the most suitable expansion possibility, given its moderate weight associated with its relatively small volume. The simulations point out the HESS mass could be reduced without decreasing the EV performance. Series battery/ultracapacitor combination offers many benefits, which make it well-suited for light EVs as efficiency and performance enhancement.

However, it is important to highlight that the results reached by this study are theoretical and the optimum configuration parameters need to be evaluated. The battery for a HESS real application should be an adequate commercial model according to the optimum theoretical values, moreover, it is possible to design a battery with a combination of cells to meet the desired voltage and capacity. The optimized EMs also need to be evaluated regarding constructive constraints and the same applies to the differential transmission

ratio, that needs to be tuned considering a manufacturable gear teeth combination.

Besides the listed limitations, this paper has shown the HESS is a suitable solution to decrease the electric vehicle overall mass, when submitted to a real urban driving scenario, that considers the road altimetry, without performance losses.

Expansions of this study may include a different real driving cycle considering more highway periods, once the storage system varies depending on different scenarios.

Acknowledgements The authors wish to thank the Brazilian Federal Agency for Support and Evaluation of Graduate Education (CAPES), the National Council for Scientific and Technological Development (CNPq), the State of São Paulo Research Foundation (FAPESP) and the University of Campinas (UNICAMP) for financial support and scholarships.

Declarations

Conflict of interest The authors declare that they have no conflict of interest.

References

- Allègre AL, Bouscayrol A, Trigui R (2013) Flexible real-time control of a hybrid energy storage system for electric vehicles. *IET Electr Syst Transport* 3(3):79
- Das A, Li D, Williams D, Greenwood D (2019) Weldability and shear strength feasibility study for automotive electric vehicle battery tab interconnects. *J Braz Soc Mech Sci Eng* 41(1):54
- Holjevac N, Cheli F, Gobbi M (2019) A simulation-based concept design approach for combustion engine and battery electric vehicles. *Proceedings of the Institution of Mechanical Engineers, Part D: Journal of Automobile Engineering* 233(7):1950
- Raggi MVK, Sodré JR (2014) Numerical simulation of carbon monoxide emissions from spark ignition engines. *J Braz Soc Mech Sci Eng* 36(1):37
- Yazdani A, Shamekhi A, Hosseini S (2015) Modeling, performance simulation and controller design for a hybrid fuel cell electric vehicle. *J Braz Soc Mech Sci Eng* 37(1):375
- Holjevac N, Cheli F, Gobbi M (2019) Multi-objective vehicle optimization: Comparison of combustion engine, hybrid and electric powertrains. *Proceedings of the Institution of Mechanical Engineers, Part D: Journal of Automobile Engineering* p. 0954407019860364
- Othaganont P, Assadian F, Auger DJ (2017) Multi-objective optimisation for battery electric vehicle powertrain topologies. *Proceedings of the Institution of Mechanical Engineers, Part D: Journal of Automobile Engineering* 231(8):1046
- Eckert JJ, Silva LC, Costa ES, Santiciolli FM, Corrêa FC, Dedini FG (2019) Optimization of electric propulsion system for a hybridized vehicle. *Mech based Des Struct Mach* 47:1–27
- Nguyen BH, German R, Trovao JPF, Bouscayrol A (2018) Real-time energy management of battery/supercapacitor electric vehicles based on an adaptation of pontryagin's minimum principle. *IEEE Trans Veh Technol* 68:203–212
- Khaligh A, Li Z (2010) Battery, ultracapacitor, fuel cell, and hybrid energy storage systems for electric, hybrid electric, fuel

- cell, and plug-in hybrid electric vehicles: state of the art. *IEEE Trans Veh Technol* 59(6):2806
11. Zhou H, Bhattacharya T, Tran D, Siew TST, Khambadkone AM (2011) Composite energy storage system involving battery and ultracapacitor with dynamic energy management in microgrid applications. *IEEE Trans Power Electron* 26(3):923
 12. Azib T, Bethoux O, Remy G, Marchand C (2011) Saturation management of a controlled fuel-cell/ultracapacitor hybrid vehicle. *IEEE Trans Veh Technol* 60(9):4127
 13. Ganley JC (2012) Design and testing of a series hybrid vehicle with an ultracapacitor energy buffer. *Proceedings of the Institution of Mechanical Engineers, Part D: Journal of Automobile Engineering* 226(7):869
 14. Nguyen B, Trovao JP, German R, Bouscayrol A (2017) An optimal control-based strategy for energy management of electric vehicles using battery/supercapacitor, in *2017 IEEE Vehicle Power and Propulsion Conference (VPPC)*, pp. 1–6. 10.1109/VPPC.2017.8330985
 15. Curti J, Huang X, Minaki R, Hori Y (2012) A simplified power management strategy for a supercapacitor/battery hybrid energy storage system using the half-controlled converter, in *IECON 2012-38th Annual Conference on IEEE Industrial Electronics Society (IEEE)*, pp. 4006–4011
 16. Yu H, Cao D (2018) Multi-objective optimal sizing and real-time control of hybrid energy storage systems for electric vehicles, in *2018 IEEE Intelligent Vehicles Symposium (IV)* (IEEE), pp. 191–196
 17. Shen J, Dusmez S, Khaligh A (2014) Optimization of sizing and battery cycle life in battery/ultracapacitor hybrid energy storage systems for electric vehicle applications. *IEEE Trans Indus Inform* 10(4):2112
 18. Ostadi A, Kazerani M (2015) A comparative analysis of optimal sizing of battery-only, ultracapacitor-only, and battery-ultracapacitor hybrid energy storage systems for a city bus. *IEEE Trans Veh Technol* 64(10):4449
 19. Eckert JJ (2018) Energy storage and control optimization for an electric vehicle. *Int J Energy Res* 42(11):3506
 20. Eckert JJ, de Alkmin Silva LC, Dedini FG, Corrêa FC (2020) Electric vehicle powertrain and fuzzy control multi-objective optimization, considering dual hybrid energy storage systems. *IEEE Trans Veh Technol* 69(4):3773
 21. Shen J, Khaligh A et al (2015) A supervisory energy management control strategy in a battery/ultracapacitor hybrid energy storage system. *IEEE Trans Transp Electr* 1(3):223
 22. Tie SF, Tan CW (2013) A review of energy sources and energy management system in electric vehicles. *Renew Sustain Energy Rev* 20:82
 23. Wang S, Zhang S, Shi D, Sun X, He J (2019) Research on instantaneous optimal control of the hybrid electric vehicle with planetary gear sets. *J Braz Soc Mech Sci Eng* 41(1):51
 24. Ates Y, Erdinc O, Uzunoglu M, Vural B (2010) Energy management of an fc/uc hybrid vehicular power system using a combined neural network-wavelet transform based strategy. *Int J Hydrogen Energy* 35(2):774
 25. Rotenberg D, Vahidi A, Kolmanovsky I (2011) Ultracapacitor assisted powertrains: modeling, control, sizing, and the impact on fuel economy. *IEEE Trans Control Syst Technol* 19(3):576
 26. Song Z, Hofmann H, Li J, Han X, Ouyang M (2015) Optimization for a hybrid energy storage system in electric vehicles using dynamic programming approach. *Appl Energy* 139:151
 27. Hu X, Murgovski N, Johannesson LM, Egardt B (2014) Comparison of three electrochemical energy buffers applied to a hybrid bus powertrain with simultaneous optimal sizing and energy management. *IEEE Trans Intell Transp Syst* 15(3):1193
 28. Yin H, Zhao C, Li M, Ma C (2015) Utility function-based real-time control of a battery ultracapacitor hybrid energy system. *IEEE Trans Indus Inf* 11(1):220
 29. Madanipour V, Montazeri-Gh M, Mahmoodi-k M (2016) Optimization of the component sizing for a plug-in hybrid electric vehicle using a genetic algorithm. *Proceedings of the Institution of Mechanical Engineers, Part D: Journal of Automobile Engineering* 230(5):692
 30. Yu H, Castelli-Dezza F, Cheli F (2017) Optimal powertrain design and control of a 2-iwd electric race car, in *Electrical and Electronic Technologies for Automotive, 2017 International Conference of (IEEE)*, pp. 1–7
 31. Shi K, Yuan X, Huang G, Liu Z (2019) Weighted multiple model control system for the stable steering performance of distributed drive electric vehicle. *J Braz Soc Mech Sci Eng* 41(4):201
 32. Liu L, Shi K, Yuan X, Li Q (2019) Multiple model-based fault-tolerant control system for distributed drive electric vehicle. *J Braz Soc Mech Sci Eng* 41(11):531
 33. Li Y, Huang X, Liu D, Wang M, Xu J (2019) Hybrid energy storage system and energy distribution strategy for four-wheel independent-drive electric vehicles. *J Clean Prod* 220:756
 34. Correa FC, Eckert JJ, Silva LC, Santiciolli FM, Costa ES, Dedini FG (2015) Study of different electric vehicle propulsion system configurations, in *Vehicle Power and Propulsion Conference (VPPC)*, *IEEE (IEEE)*, pp. 1–6
 35. Eckert JJ, Silva LC, Costa ES, Santiciolli FM, Dedini FG, Corrêa FC (2017) Electric vehicle drivetrain optimisation. *IET Electr Syst Transp* 7(1):32
 36. Shen P, Zhao Z, Li J, Guo Q (2019) Development of adaptive gear shifting strategies of automatic transmission for plug-in hybrid electric commuting vehicle based on optimal energy economy. *Proceedings of the Institution of Mechanical Engineers, Part D: Journal of Automobile Engineering* p. 0954407019864209
 37. Oliveira AM, Bertoti E, Eckert JJ, Yamashita RY, dos Santos Costa E, Silva LCA, Dedini FG (2016) Evaluation of energy recovery potential through regenerative braking for a hybrid electric vehicle in a real urban drive scenario
 38. Gillespie TD (1992) *Fundamentals of vehicle dynamics* (Society of Automotive Engineers - SAE)
 39. Jazar RN (2008) *Vehicle dynamics: theory and application*. Springer Science and Business Media, New York
 40. Eckert JJ, Santiciolli FM, Bertoti E, Costa EdS, Corrêa FC, Silva LCDAE, Dedini FG (2018) Gear shifting multi-objective optimization to improve vehicle performance, fuel consumption, and engine emissions. *Mech Based Des Struct Mach* 46(2):238
 41. Eckert J, Santiciolli F, Yamashita R, Correa F, Silva LC, Dedini F (2019) Fuzzy gear shifting control optimization to improve vehicle performance, fuel consumption and engine emissions. *IET Control Theor Appl* 13:2658–2669
 42. Barbosa TP, Eckert JJ, Silva LCA, da Silva LAR, Gutiérrez JCH, Dedini FG (2020) Gear shifting optimization applied to a flex-fuel vehicle under real driving conditions. *Mech Based Des Struct Mach* 25:1–18
 43. da Silva SF, Eckert JJ, Silva FL, Silva LC, Dedini FG (2021) Multi-objective optimization design and control of plug-in hybrid electric vehicle powertrain for minimization of energy consumption, exhaust emissions and battery degradation. *Energy Convers Manag* 234:2356
 44. Eckert JJ, Santiciolli FM, Silva LC, Costa ES, Corrêa FC, Dedini FG (2016) Co-simulation to evaluate acceleration performance and fuel consumption of hybrid vehicles. *J Braz Soc Mech Sci Eng* 25:1–14
 45. Tong W (2014) *Mechanical design of electric motors*. CRC Press, Boca Raton

46. Rotering N, Ilic M (2011) Optimal charge control of plug-in hybrid electric vehicles in deregulated electricity markets. *Power Syst, IEEE Trans on* 26(3):1021
47. Ghafouryan MM, Ataei S, Dastjerd FT (2016) A novel method for the design of regenerative brake system in an urban automotive. *J Braz Soc Mech Sci Eng* 38(3):945
48. Lu D, Ouyang M, Gu J, Li J (2014) Instantaneous optimal regenerative braking control for a permanent-magnet synchronous motor in a four-wheel-drive electric vehicle. *Proceedings of the Institution of Mechanical Engineers, Part D: Journal of Automobile Engineering* 228(8):894
49. Suntharalingam P, Economou JT, Knowles K (2017) Kinetic energy storage using a dual-braking system for an unmanned parallel hybrid electric vehicle. *Proceedings of the Institution of Mechanical Engineers, Part D: Journal of Automobile Engineering* 231(10):1353
50. Thackeray MM, Wolverton C, Isaacs ED (2012) Electrical energy storage for transportation - approaching the limits of, and going beyond, lithium-ion batteries. *Energy Environ Sci* 5(7):7854
51. Wang CY, Zhang G, Ge S, Xu T, Ji Y, Yang XG, Leng Y (2016) Lithium-ion battery structure that self-heats at low temperatures. *Nature* 529(7587):515
52. Young K, Wang C, Wang LY, Strunz K (2013) Electric vehicle battery technologies, in *electric vehicle integration into modern power networks*. Springer, New York, pp 15–56
53. Diouf B, Pode R (2015) Potential of lithium-ion batteries in renewable energy. *Renew Energy* 76:375
54. Zhang X, Mi C (2011) *Vehicle power management: modeling, control and optimization*. Springer Science and Business Media, New York
55. Corrêa FC, Eckert JJ, Santiciolli FM, Silva LC, Costa ES, Dedini FG (2017) Electric vehicle battery-ultracapacitor energy system optimization, in *Vehicle Power and Propulsion Conference (VPPC), IEEE (IEEE)*, pp. 1–6
56. Ravey A, Roche R, Blunier B, Miraoui A (2012) Combined optimal sizing and energy management of hybrid electric vehicles, in *2012 IEEE Transportation Electrification Conference and Expo (ITEC) (IEEE)*, pp. 1–6
57. Yang J, Wang W, Ma K, Yang B (2019) Optimal dispatching strategy for shared battery station of electric vehicle by divisional battery control. *IEEE Access* 7:38224
58. Prochazka P, Cervinka D, Martis J, Cipin R, Vorel P (2016) Li-ion battery deep discharge degradation. *ECS Trans* 74(1):31
59. Silva LC, Eckert JJ, Santiciolli FM, Costa ES, Dedini FG, Corrêa FC (2015) A study of battery power for a different electric vehicle propulsion system, in *International Conference on Electrical Systems for Aircraft, Railway, Ship Propulsion and Road Vehicles (ESARS)*
60. Martínez JS, Mulot J, Harel F, Hissel D, Péra MC, John RI, Amiet M (2013) Experimental validation of a type-2 fuzzy logic controller for energy management in hybrid electrical vehicles. *Eng Appl Artif Intell* 26:1772
61. Ma T, Yang H, Lu L (2015) Development of hybrid battery-supercapacitor energy storage for remote area renewable energy systems. *Appl Energy* 153:56
62. Zhang S, Xiong R, Cao J (2016) Battery durability and longevity based power management for plug-in hybrid electric vehicle with hybrid energy storage system. *Appl energy* 179:316
63. Wang B, Xu J, Cao B, Zhou X (2015) A novel multimode hybrid energy storage system and its energy management strategy for electric vehicles. *J Power Sour* 281:432
64. Trovão JP, Pereira PG, Jorge HM, Antunes CH (2013) A multi-level energy management system for multi-source electric vehicles—an integrated rule-based meta-heuristic approach. *Appl Energy* 105:304
65. Veneri O, Capasso C, Patalano S (2018) Experimental investigation into the effectiveness of a super-capacitor based hybrid energy storage system for urban commercial vehicles. *Appl Energy* 227:312
66. Eckert JJ, Santiciolli FM, Silva LCA, Corrêa FC, Dedini FG (2020) Design of an aftermarket hybridization kit: Reducing costs and emissions considering a local driving cycle. *Vehicles* 2(1):210
67. Gen M, Cheng R, Lin L (2008) *Network models and optimization: multiobjective genetic algorithm approach*. Springer Science and Business Media, New York
68. Eckert JJ, Santiciolli FM, Silva LC, Dedini FG (2021) Vehicle drivetrain design multi-objective optimization. *Mech Mach Theor* 156:104123
69. Lopes MV, Eckert JJ, Martins TS, Santos AA (2020) Optimizing strain energy extraction from multi-beam piezoelectric devices for heavy haul freight cars. *J Braz Soc Mech Sci Eng* 42(1):1

Publisher's Note Springer Nature remains neutral with regard to jurisdictional claims in published maps and institutional affiliations.